Ceramics International 45 (2019) 19538–19541

Contents lists available at ScienceDirect

Ceramics International

journal homepage: www.elsevier.com/locate/ceramint

Short communication

Suppressed secondary phase generation in thermoelectric higher manganese silicide by fabrication process optimization

Gwansik Kim[a,1], Hyun Jun Rim[a,1], Kyu Hyoung Lee[a], Jong Wook Roh[b,**], Wooyoung Lee[a,*]

[a] Department of Materials Science and Engineering, Yonsei University, Seoul, 03722, South Korea
[b] School of Nano & Materials Science and Engineering, Kyungpook National University, Gyeongsangbuk-do, 37224, Republic of Korea

ARTICLE INFO

Keywords:
Thermoelectricity
Higher manganese silicide
Secondary phase
Solid-state reaction
Arc melting

ABSTRACT

Controlling the generation of secondary phases in thermoelectric higher manganese silicides is crucial to enhance their thermoelectric performance for use in automotive thermoelectric generators. However, the effect of different synthesis and sintering procedures on the secondary phase formation and thermoelectric properties has not yet been investigated. In this study, we demonstrate that fabricating $Mn_{11}Si_{19}$ via arc melting and spark plasma sintering results in a figure of merit (ZT) of 0.43 at 823 K, which is 15% higher than for a sample fabricated by a solid-state reaction and spark plasma sintering. We found that the presence of secondary MnSi phases in the $Mn_{11}Si_{19}$ samples was significantly reduced when using arc melting instead of solid-state reaction, which suggests that the phase formation behavior could be controlled by optimizing the fabrication process.

1. Introduction

Thermoelectric (TE) technologies, which allow direct conversion between heat and electricity, present a strategy to solve the energy efficiency problems. The TE performance is directly determined by the dimensionless figure of merit $ZT = \sigma S^2 T/\kappa_{tot}$, where σ, S, κ_{tot}, and T represent the electrical conductivity, Seebeck coefficient, total thermal conductivity, and absolute temperature, respectively. The total thermal conductivity κ_{tot} consists of the electronic thermal conductivity κ_{ele} and the lattice thermal conductivity κ_{lat} [1]. Silicide-based TE materials are promising candidates for TE generators because they are abundant and environmentally friendly. In particular, higher manganese silicides (HMS, $MnSi_x$ ($1.70 < x < 1.75$)), which are considered as a representative of p-type silicides, exhibit reasonably high electronic transport properties at temperatures of 500–800 K [2,3]. Furthermore, HMS (11.0–13.0 $\times 10^{-6}\,K^{-1}$) have similar intrinsic characteristics and thermal expansion coefficients as the currently used n-type Mg_2Si (Mg_2Si: 13.0 $\times 10^{-6}\,K^{-1}$ and $Mg_2Si_{1-x}Sn_x$: 17.0 $\times 10^{-6}\,K^{-1}$) [4–6], indicating that they are suitable for the fabrication of silicide-based TE modules. HMS are also mechanically reliable (1.63 MPa $m^{1/2}$) and chemically stable at high temperatures [6,7].

For practical applications, it is crucial to fabricate HMS bulk samples with optimal TE properties. However, the reported ZT of state-of-the-art HMS, ~0.4, is still relatively low. For example, Sadia et al. obtained a ZT of ~0.42 at 723 K for p-type Mn_4Si_7 synthesized by arc melting and hot pressing [8]. An et al. synthesized p-type $Mn_{27}Si_{47}$ and achieved a maximum ZT of 0.41 at 850 K using various sintering conditions [9]. The low ZT values of HMS are mainly caused by metallic MnSi secondary phases present in the HMS matrix, which result in a drastic reduction of the Seebeck coefficient and an increase in the thermal conductivity [10].

In this study, we obtained polycrystalline bulk HMS with high homogeneity and a maximum ZT of 0.43 at 823 K by optimizing the fabrication process. For this, we compared solid-state reaction (SSR) and arc melting (AM) synthesis methods in combination with either hot press (HP) or spark plasma sintering (SPS). We found that the metallic MnSi secondary phase was most significantly reduced when using AM and SPS together resulting in the best TE properties. Our findings demonstrate the importance of controlling the secondary phase and optimizing the synthesis process of HMS materials for TE applications.

2. Materials and methods

To compare the microstructure and thermoelectric properties of $Mn_{11}Si_{19}$ samples prepared using different synthesis methods, they were prepared using solid-state reaction (SSR) and arc melting (AM). The Mn powder (99.95%, Alfa Aesar), Si powder (99.9%, Alfa Aesar), Mn granule (99.98%, Alfa Aesar), and Si granule (99.9999%, Alfa

* Corresponding author.
** Corresponding author.
E-mail addresses: jw.roh@knu.ac.kr (J.W. Roh), wooyoung@yonsei.ac.kr (W. Lee).
[1] These authors contributed equally.

https://doi.org/10.1016/j.ceramint.2019.06.104
Received 3 April 2019; Received in revised form 3 June 2019; Accepted 11 June 2019
Available online 12 June 2019

Aesar) were weighed in the appropriate ratios to achieve the nominal composition of $Mn_{11}Si_{19}$. For the SSR, the powders were mixed for 1 h in a glove box using an agate mortar. Then, the mixed powders were vacuum-sealed in a quartz tube and annealed in a box furnace at 1323 K for 48 h. For the AM, the precursor solids of Mn and Si were placed in an inverted dome base within a dynamically vacuumed arc chamber and were consecutively melted under Ar atmosphere to achieve a homogeneous composition. The obtained samples were ground into powders using an agate mortar and sieved to obtain particle sizes smaller than 53 μm. Then, the disc-type HMS polycrystalline bulks (25 mm diameter and 6 mm thickness) were compacted by either hot press (HP) or spark plasma sintering (SPS). The sintering time of SPS and HP were 5 min and 1 or 2 h, respectively, at a temperature of 1193 K and pressure of 60 MPa.

A phase analysis of the powders and compacted bulks was carried out using X-ray diffraction (Ultima IV/ME 200DX, Rigaku, Japan) with CuKα radiation. The wt.% of the secondary phases was calculated by Rietveld refinement. The microstructure of the compacted bulks was investigated by scanning electron microscopy (SEM, JEOL-7800F, JEOL Ltd., Japan). The temperature dependence of the electrical conductivity σ and the Seebeck coefficient S were evaluated in the range of 300–873 K using a system measuring thermoelectric properties (ZEM-3, ULVAC, Japan). Hall measurements were carried out using home-made system under a 1T magnetic field in the van der Pauw configuration at room temperature. The κ_{tot} values were calculated using the equation $\kappa = \rho \cdot C_p \cdot \lambda$, where ρ is the density, C_p is the specific heat capacity, and λ is the thermal diffusivity. To measure λ and C_p as a function of temperature under vacuum, the laser flash method (Netszch LFA-457, Germany) and differential scanning calorimetry (DSC 8000, PerkinElmer, USA) were used.

3. Results and discussion

To investigate which combination of synthesis and sintering method would result in the best TE properties, we prepared $Mn_{11}Si_{19}$ samples using the combination of synthesis (SSR and AM) and sintering method (SPS and HP).

To compare the effects of the different synthesis and sintering methods on the phases present in the resulting $Mn_{11}Si_{19}$, we performed XRD analysis on the powders and the compacted bulks (Fig. 1). In previous reports, the XRD measurements revealed that the samples mainly included phases of Mn_4Si_7, $Mn_{11}Si_{19}$, $Mn_{15}Si_{26}$, and $Mn_{27}Si_{47}$ [11]. The Mn and Si sub-lattices were incommensurate along the c-axis with lattice parameters varying from 17 Å (Mn_4Si_7) to 118 Å ($Mn_{27}Si_{47}$). All phases exhibited similar lattice parameters of approximately 5.5 Å along the a- and b-axis due to the dependence to the Mn sub-lattice [12].

All samples have a tetragonal crystal structure, specifically known as the Nowotny chimney ladder phase, and MnSi and Si secondary phases are present. The AM and AM/SPS samples exhibited significantly lower proportions of the secondary phases MnSi and Si compared to that of the SSR-synthesized samples. Using Rietveld refinement, the amount of MnSi secondary phase was calculated to be 0.5–1.0 wt% in the AM-synthesized and 3.0–5.5 wt% in the SSR-synthesized samples.

This is likely because achieving a uniform phase using SSR is experimentally difficult due to unpredictable experimental parameters, such as various powder sizes, unsteady temperature distributions, and different atomic diffusion rates for Mn and Si, resulting in the degradation of TE properties [13]. Moreover, the presence of undiffused Si, induced by the slow diffusion rate of Si atoms, may have formed the MnSi and Si secondary phases in the HMS matrix of the SSR-synthesized samples [8]. In contrast, AM is based on a secondary melting process, which can minimize the segregation by completely melting the precursor ingots [14]. Also, the cooling rate of the AM process is faster than that of the SSR process, which can prevent the phase segregation

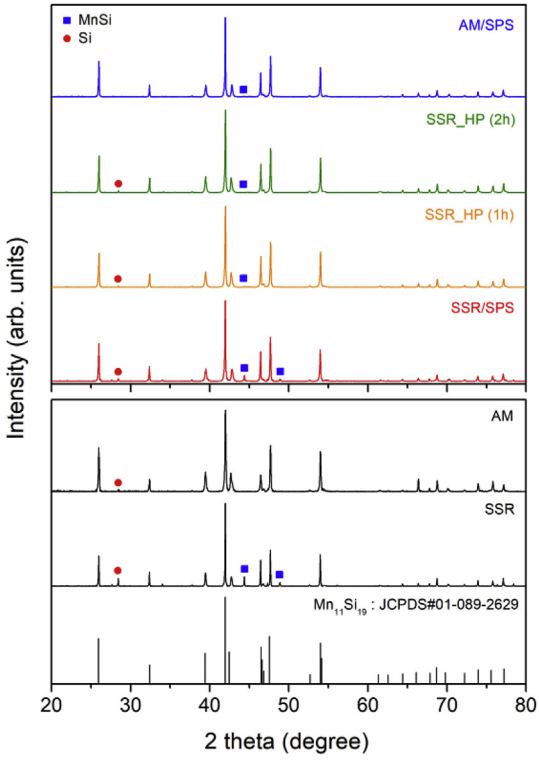

Fig. 1. XRD patterns of the $Mn_{11}Si_{19}$ samples prepared by SSR, AM, SSR/SPS, SSR/HP (1 h), SSR/HP (2 h), and AM/SPS. The blue squares indicate secondary MnSi phases and the red dots secondary Si phases. (For interpretation of the references to colour in this figure legend, the reader is referred to the Web version of this article.)

of the MnSi and Si phases.

To compare the presence of secondary phases in the SPS and HP sintering processes, we analyzed the XRD patterns of the SSR/SPS and the SSR/HP (1 h) samples using Rietveld refinement. We calculated the MnSi secondary phase content of the SSR/HP (1 h) sample to be 1.0–1.5 wt% and that of the SSR/SPS sample to be 2.5–3.5 wt%. This shows that a smaller amount of the MnSi secondary phase was generated using the long HP sintering process (1–2 h). However, once formed in the SSR reaction, HP sintering was insufficient in removing the secondary phases considering that MnSi was still present in the SSR/HP (1 h) and SSR/HP (2 h) samples.

To reveal the microstructure of the SSR/SPS, SSR/HP (1 h), and AM/SPS samples, we performed SEM analysis (Fig. 2). The SSR/SPS sample showed the highest porosity (Fig. 2 (a) and (b)), which was lower for the SSR/HP (1 h) and AM/SPS samples (Fig. 2 (c) and (d), and (e) and (f), respectively). The porosity is a characteristic that can be detrimental to the TE properties. This is because the presence of closed pores may result in hole scattering, which decreases σ.

To analyze the temperature dependency of the electronic transport properties of the SSR/SPS, SSR/HP(1 h), SSR/HP(2 h) and AM/SPS samples, we measured their σ and S values as a function of temperature between 300 and 873 K (Fig. 3 (a)). In the temperature range under 800 K, we observed a decrease of σ with temperature for all samples, suggesting a degenerate transport behavior of the HMS. This is likely due to electron acoustic phonon scattering, which becomes more significant with increasing temperature. It leads to a reduction in the carrier mobility, and thus, decreased σ values. Additionally, the slight increase of σ above 830 K seemed to be due to bipolar transport in HMS. Moreover, we found that the SSR/SPS sample exhibited a lower σ compared to the AM/SPS and SSR/HP samples, which is likely due to its higher proportion of secondary phases and higher level of porosity. This is in agreement with studies on MnSi and Si secondary phases formed

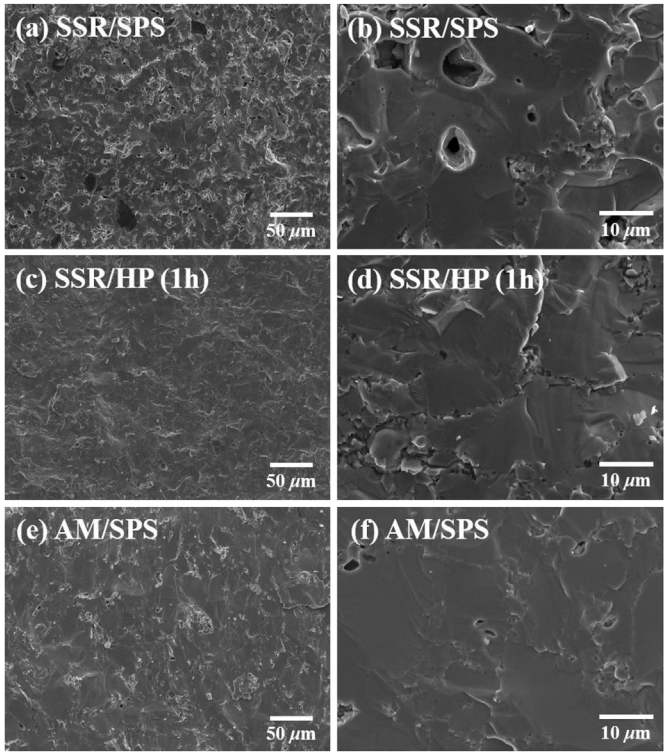

Fig. 2. SEM images of the SSR/SPS (a) and (b), SSR/HP (1 h) (c) and (d), and AM/SPS samples (e) and (f) at magnifications of 50 μm (left column) and 10 μm (right column).

by peritectic solidification from solid MnSi and liquid HMS, which exhibit low σ due to the intensified hole scattering at the interfaces between the HMS matrix and the secondary phases [3,8,15].

To clarify this, we calculated the carrier concentration (p_H) and mobility (μ_{Hall}) estimating a one band model (Table 1). We found similar p_H values of 1.52×10^{21}–1.54×10^{21} cm^{-3} for the SSR/SPS and AM/SPS samples. In contrast, the μ_{Hall} value of the AM/SPS sample (2.43 cm^2 V^{-1} s^{-1}) was higher than that of the SSR/SPS sample (2.19 cm^2 V^{-1} s^{-1}), indicating that the holes (h^+) were scattered at the interfaces between the HMS matrix and the secondary phases.

The absolute S values of the SSR/SPS and SSR/HP (1 h) samples were similar (225 μV K^{-1} and 228 μV K^{-1} at 773 K) and lower than that of the AM/SPS sample (230 μV K^{-1} at 773 K). The metallic properties of the MnSi secondary phase in the SSR/SPS and SSR/HP samples may result in a decrease in the S values. Consequently, the calculated power factor (σS^2) values of the AM/SPS sample (1.50 mW m^{-1} K^{-2}) and SSR/HP samples (1.60 mW m^{-1} K^{-2}) were higher than that of the SSR/SPS sample (1.34 mW m^{-1} K^{-2}, Fig. 3 (b)).

In order to further investigate the TE properties of the SSR/SPS, SSR/HP(1 h), SSR/HP(2 h) and AM/SPS samples, we then investigated their thermal conductivities κ_{tot} (filled symbols) and κ_{lat} (unfilled symbols) as a function of temperature (Fig. 4(a)). κ_{lat} was calculated by subtracting the electronic contribution (κ_{ele}) from κ_{tot}. The Lorenz number (L) was estimated using the following equation [16]:

$$L = \left(\frac{k_B}{e}\right)^2 \left(\frac{\left(r + \frac{7}{2}\right) F_{r+\frac{5}{2}}(\eta)}{\left(r + \frac{3}{2}\right) F_{r+\frac{1}{2}}(\eta)} - \left[\frac{\left(r + \frac{5}{2}\right) F_{r+\frac{3}{2}}(\eta)}{\left(r + \frac{3}{2}\right) F_{r+\frac{1}{2}}(\eta)} \right]^2 \right),$$

where η is the Fermi energy, $F_n(\eta)$ is the n-th order Fermi integral, and r is the scattering parameter. The calculated L values ranged from 1.6×10^{-8} V^2 K^{-2} to 2.0×10^{-8} V^2 K^{-2}. The κ_{tot} values (2.82 W m^{-1} K^{-1} at 373 K and 2.92 W m^{-1} K^{-1} at 873 K) of the SSR/SPS sample were lower than that of the other samples (AM/SPS: 2.87 W m^{-1} K^{-1} at 373 K and 2.95 W m^{-1} K^{-1} at 873 K; SSR/HP (1 h): 2.93 W m^{-1} K^{-1} at 373 K and 2.97 W m^{-1} K^{-1} at 873 K) due to its low density. Although the metallic MnSi secondary phase caused an increase in thermal conductivity, the κ_{lat} of all samples were reduced because of the intensified phonon scattering at the interfaces between the HMS and MnSi or the pores in the matrix. Moreover, we found that the SSR/HP samples had the highest κ_{tot} values. This was likely induced by the MnSi secondary phase taking into account that the AM/SPS sample exhibited a similar experimental density.

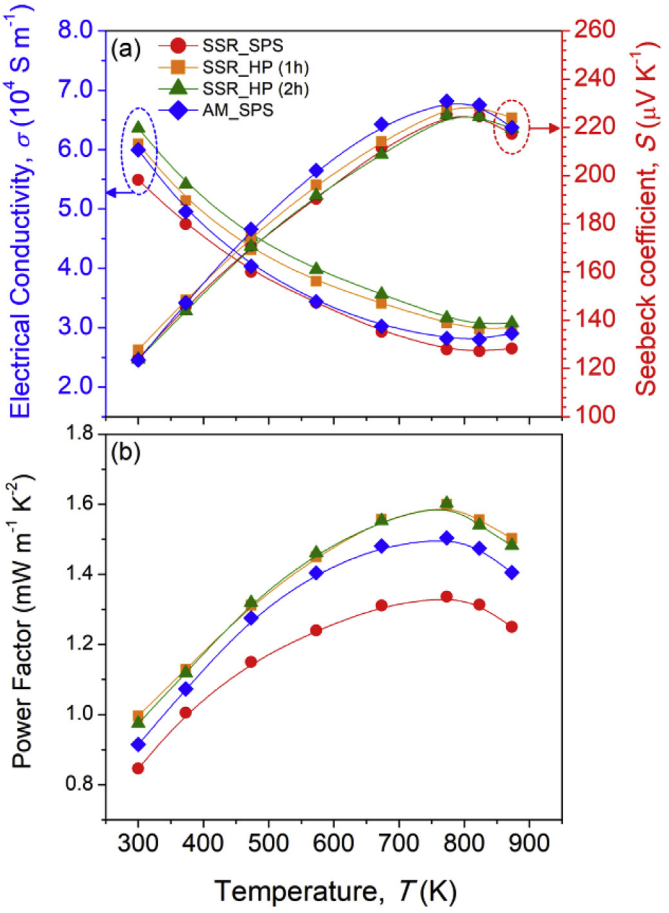

Fig. 3. Temperature dependence of the electrical conductivity σ and the Seebeck coefficient S (a), as well as of the power factor (b) for the SSR/SPS, SSR/HP (1 h), SSR/HP (2 h), and AM/SPS samples.

Table 1
Room-temperature electronic transport parameters of two $Mn_{11}Si_{19}$ samples.

	σ (S m^{-1})	S (μV K^{-1})	p_H (cm^{-3})	μ_{Hall} (cm^2 V^{-1} s^{-1})
SSR/SPS	54901.89	124.14	1.54×10^{21}	2.19
AM/SPS	59961.96	123.50	1.52×10^{21}	2.43

Together with the values for the power factor and the thermal conductivities, we were able to calculate the dimensionless figure of merit ZT for the samples (Fig. 4 (b)). We found that the SSR/HP (1 h), SSR/HP (2 h), and AM/SPS samples achieved high ZTs of 0.43–0.45 at 823 K, which is 15% higher than that of the SSR/SPS sample.

4. Conclusions

In summary, we were able to successfully control secondary phase generation in thermoelectric $Mn_{11}Si_{19}$ by optimizing its fabrication process. The AM process suppressed the formation of MnSi and Si phases more effectively than the SSR method due to the rapid cooling

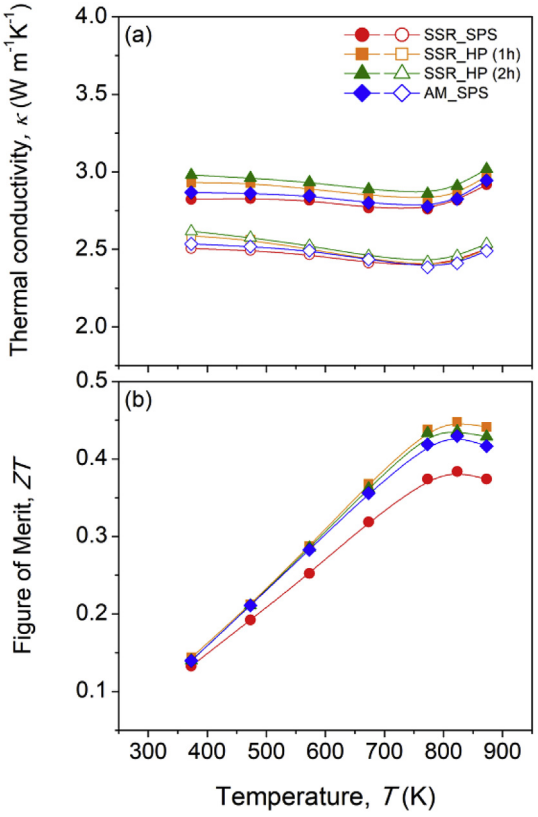

Fig. 4. Temperature dependence of the total thermal conductivity κ_{tot} (filled symbols) and the lattice thermal conductivity κ_{lat} (unfilled symbols, a), and of the dimensionless figure of merit *ZT* (b) for the SSR/SPS, SSR/HP (1 h), SSR/HP (2 h), and AM/SPS samples.

rate. By decreasing the presence of secondary phases, we improved the electronic transport properties and manipulated thermal transport properties. As a result, we obtained the highest *ZT* of 0.43 at 823 K for the AM/SPS sample, which is 15% higher than that of the SSR/SPS sample. Our results demonstrate that the presence of secondary phases plays an important role in the charge and energy transport properties of HMS. Optimizing the fabrication process of HMS to reduce secondary phase formation offers an accessible route to improving their TE properties.

Acknowledgements

This work was supported by the National Research Foundation of Korea (NRF) Grant (2017R1A2A1A17069528) and Priority Research Centers Program (2019R1A6A1A11055660).

References

[1] G.J. Snyder, E.S. Toberer, Complex thermoelectric materials, Nat. Mater. 7 (2008) 105–114.
[2] M.I. Fedorov, G.N. Isachenko, Silicides: materials for thermoelectric energy conversion, Jpn. J. Appl. Phys. 54 (2015) 07JA05.
[3] Z. Li, J.F. Dong, F.H. Sun, S. Hirono, J.F. Li, Significant enhancement of the thermoelectric performance of higher manganese silicide by incorporating MnTe nanophase derived from Te nanowire, Chem. Mater. 27 (2017) 7378–7389.
[4] Y. Kikuchi, T. Nakajo, K. Hayashi, Y. Miyazaki, High temperature X-ray diffraction study on incommensurate composite crystal $MnSi_{\gamma}$ – (3 + 1)-dimensional superspace approach, J. Alloy. Comp. 616 (2014) 263–267.
[5] M. Imai, Y. Isoda, H. Udono, Thermal expansion of semiconducting silicides β-$FeSi_2$ and Mg_2Si, Intermetallics 66 (2015) 127–132.
[6] Y. Gelbstein, J. Tunbridge, R. Dixon, M.J. Reece, H. Ning, R. Gilchrist, R. Summers, I. Agote, M.A. Lagos, K. Simpson, C. Rouaud, P. Feulner, S. Rivera, R. Torrecillas, M. Husband, J. Crossley, I. Rombinson, Physical, mechanical, and structural properties of highly efficient nanostructured n- and p-silicides for practical thermoelectric applications, J. Electron. Mater. 43 (2014) 1703–1711.
[7] X. She, X. Su, H. Du, T. Liang, G. Zheng, Y. Yan, R. Akram, C. Uher, X. Tang, High thermoelectric performance of higher manganese silicides prepared by ultra-fast thermal explosion, J. Mater. Chem. C 3 (2015) 12116–12122.
[8] Y. Sadia, Z. Aminov, D. Mogilyansky, Y. Gelbstein, Texture anisotropy of higher manganese silicide following arc-melting and hot-pressing, Intermetallics 68 (2016) 71–77.
[9] T.H. An, S.M. Choi, W.S. Seo, C. Park, I.H. Kim, S.U. Kim, The effect of microstructure on the thermoelectric properties of polycrystalline higher manganese silicides, Jpn. J. Appl. Phys. 52 (2013) 10MC11.
[10] S. Muthiah, R.C. Singh, B.D. Pathak, P.K. Avasthi, R. Kumar, A. Kumar, A.K. Srivastava, A. Dhar, Significant enhancement in thermoelectric performance of nanostructured higher manganese silicides synthesized employing a melt spinning technique, Nanoscale 10 (2018) 1970–1977.
[11] W.D. Liu, Z.G. Chen, J. Zou, Eco-friendly higher manganese silicide thermoelectric materials: progress and future challenges, Adv. Energy Mater. 8 (2018) 1800056.
[12] X. Chen, J. Zhou, J.B. Goodenough, L. Shi, Enhanced thermoelectric power factor of Re-substituted higher manganese silicides with small islands of MnSi secondary phase, J. Mater. Chem. C 3 (2015) 10500–10508.
[13] A.R. West, Solid State Chemistry and its Applications, Wiley & Sons, 2005.
[14] K.O. Yu, Modeling for Casting & Solidification Processing, CRC, 2001.
[15] S.N. Girard, X. Chen, F. Meng, A. Pokhrel, J. Zhou, L. Shi, S. Jin, Thermoelectric properties of undoped high purity higher manganese silicides grown by chemical vapor transport, Chem. Mater. 26 (2014) 5097–5104.
[16] L.D. Zhao, S.H. Lo, J.Q. He, H. Li, K. Biswas, J. Androulakis, C.I. Wu, T.P. Hogan, D.Y. Chung, V.P. Dravid, M.G. Kanatzidis, High performance thermoelectrics from earth-abundant materials: enhanced figure of merit in PbS by second phase nanostructures, J. Am. Chem. Soc. 133 (2011) 20476–20487.